JOURNAL OF GEOPHYSICAL RESEARCH: OCEANS, VOL. 118, 3490–3506, doi:10.1002/jgrc.20256, 2013

Spatial variability of the wave bottom boundary layer over movable rippled beds

S. Rodríguez-Abudo,[1] D. L. Foster,[1,2] and M. Henriquez[3]

Received 20 July 2012; revised 24 May 2013; accepted 28 May 2013; published 19 July 2013.

[1] Observations of the spatially dependent velocity field over movable bed forms subjected to slightly skewed and asymmetric regular wave forcing were collected. The dynamics between the ripple elements is dominated by coherent vortices, characterized by the swirling strength, and evidenced in the temporal and spectral characterization. Within the boundary layer, spectral energy in the second harmonic ($3f_0$) is amplified at the ripple slopes and is consistent with the location of the expected strongest pressure gradients. First-moment and second-moment velocity statistics were used to address the spatial variability of the intra-ripple hydrodynamics. Estimates of displacement and momentum thicknesses (δ^* and δ_{mom}) are smaller than suggested by the higher harmonics, but consistently highlight areas of adverse and favorable pressure gradients. Shear stress and roughness estimates were inferred by fitting a logarithmic model to first-moment and second-moment statistics of the velocity field. The maximum Shields parameter was observed to peak at the stoss slope of asymmetric ripples during the strongest and shorter half-wave period (onshore). First-moment roughness estimates are similar in magnitude to bed load parameterizations provided by Li et al. (1997), and about a factor of 3 larger than second-moment estimates. Assessment of the vertical transfer of horizontal momentum derived using a Reynolds decomposition suggests that stresses inferred from the logarithmic law using first-moment velocity statistics appropriately reproduce the mean momentum transfer for the longer and weaker offshore half-wave period.

Citation: Rodríguez-Abudo, S., D. L. Foster, and M. Henriquez (2013), Spatial variability of the wave bottom boundary layer over movable rippled beds, *J. Geophys. Res. Oceans*, *118*, 3490–3506, doi:10.1002/jgrc.20256.

1. Introduction

[2] In the coastal ocean, the initiation of sediment transport occurs in the wave bottom boundary layer (WBBL), as sediment particles mobilize when a critical threshold in the shear stress and/or horizontal pressure gradient is exceeded [*Shields*, 1936; *Sleath*, 1999]. On a flat sediment bed, shear stress acts via skin friction, the name collectively given to viscous stresses acting on sediment grains plus pressure drag imparted by each individual grain [*Fredsøe and Deigaard*, 1992; *Maddux et al*., 2003]. On a rippled bed, the large roughness elements enhance vortex formation and ejection [*Bagnold*, 1946; *Van der Werf et al*., 2007; *Nichols and Foster*, 2007], further complicating momentum transfer in the WBBL. Due to the turbulent nature of the flow, the unsteadiness of the free stream, and the spatial nonuniformity imposed by the rippled bed, the shear stress is often parameterized with empirical and quasi-empirical formulations (for a review see *Nielsen* [1992] and *Fredsøe and Deigaard* [1992]). Parameterizations are often based on bulk flow estimates and not generally derived from direct estimates of the bottom boundary layer dynamics. Furthermore, the formulations lack a detailed spatial characterization of the relative contributions of the individual mechanisms.

[3] Early formulations of shear stress and bed roughness were largely based on field observations of flow velocity outside the WBBL [*Drake and Cacchione*, 1986; *Drake et al*., 1992]. The WBBL is characterized by a reduction in velocity magnitude and a phase lead near the sea bed [*Trowbridge and Agrawal*, 1995; *Foster et al*., 2000]. Most detailed field scale observations of fluid-sediment interactions in the coastal ocean have primarily been limited to one-dimensional profiles mainly outside the WBBL [*Osborne and Vincent*, 1996; *Traykovski et al*., 1999; *Foster et al*., 2000; *Crawford and Hay*, 2001; *Doucette*, 2002; *Smyth et al*., 2002; *Thorne and Hanes*, 2002; *Chang and Hanes*, 2004]. Recent two-dimensional (2-D) field observations of the flow field in the lower water column obtained by *Doron et al*. [2000] and *Nimmo Smith et al*. [2005]

[1]Center for Ocean Engineering, University of New Hampshire, Durham, New Hampshire, USA.
[2]Department of Mechanical Engineering, University of New Hampshire, Durham, New Hampshire, USA.
[3]Department of Hydraulic Engineering, Delft University of Technology, Delft, Netherlands.

Corresponding author: S. Rodríguez-Abudo, Center for Ocean Engineering, University of New Hampshire, 24 Colovos Rd., Durham, NH 03824, USA. (s.rodriguez-abudo@wildcats.unh.edu)

2169-9275/13/10.1002/jgrc.20256

provided significant insight on the anisotropic nature of the boundary layer and its role in wave energy dissipation, yet they lacked information very close to the bed (O(1) cm).

[4] After the early efforts of *Darwin* [1883], *Ayrton* [1910], and *Bagnold* [1946], most detailed observations of the WBBL over rippled beds have been obtained in oscillatory flow tunnels. Over fixed rippled beds, *Jonsson and Carlsen* [1976] observed boundary layer thicknesses and estimated friction factors, while *Ahmed and Sato* [2001] reported flow separation from 2-D velocity observations. Over movable sediment beds, the occurrence, growth, and evolution of sand ripples has been shown to be dependent on the initial conditions and inconsistent with an equilibrium formulation [*O'Donoghue and Clubb*, 2001; *O'Donoghue et al*., 2006; *Doucette and O'Donoghue*, 2006b].

[5] In a wave flume investigation, with vertical orbital motions and a fixed rippled bed, *Fredsøe et al*. [1999] showed that even in combined wave-current flows, coherent vortices dominate the near bed dynamics, resulting in an increase of one order of magnitude in the apparent roughness as opposed to currents alone. Similarly, but at a slightly larger scale, *Davies and Thorne* [2005] identified the primary sediment entraining mechanism under monochromatic waves as a lee vortex that ejects during flow reversal; while *Nichols and Foster* [2007] and *Nichols and Foster* [2009] found correlation between these events, ripple geometry, and irregular wave forcing conditions. Field observations of *Traykovski et al*. [1999] suggest that vortex shedding may be responsible for a net offshore transport of suspended sediment, while *Smyth et al*. [2002] showed it is the dominant process suspending and distributing sediments in environments dominated by irregular and cross ripples.

[6] It is, therefore, expected that the well-known processes responsible for imparting shear stress on a flat bed, and the boundary layer theory used to assess them, differ drastically from form-induced vortex-dominated WBBLs. In this effort, we aim to assess the validity of characterizing such processes with extensions of theories for turbulent flows over rough walls. In section 2, we provide new detailed 2-D observations of the flow field within the WBBL over a mobile rippled bed with strong evidence of vortex signatures. Bulk statistics, temporal variability, and spectral behavior of the flow are provided in sections 3–5. We use an integral approach to examine the spatially variable boundary layer thickness in section 6, and compute the viscous stress in section 7. Using a logarithmic layer approach, inferences of spatially dependent shear stress and bed roughness are provided in section 8. We discuss the validity and applicability of this approach in section 9.

2. Observations

2.1. Facility

[7] The observational data for this study was collected in a small-scale (1:15) wave flume at the Fluid Mechanics Laboratory at Delft University of Technology, the Netherlands. The flume is 42 m long, 0.8 m wide, and 1 m high. A 1:20 rigid slope starting 32 m from the wave generator was covered with sediment extending to a few meters from the wave generation area. The wave generator is capable of producing regular waves, 5 cm in height, and 2 s in wave period as observed 29 m from the wave generator in 31 cm water depth. Additional wave characteristics are summarized in Table 1. The active reflection compensation system reduced the effect of reflected waves (its mechanisms are

Table 1. Summary of Experimental Parameters

Parameter	Value
Wave height, H	5 cm
Wave period, T	2 s
Wavelength, λ	3.3 m
Horizontal velocity amplitude, u_0	11.8 cm s^{-1}
Horizontal velocity amplitude onshore, $u_{0,\mathrm{on}}$	13.2 cm s^{-1}
Horizontal velocity amplitude offshore, $u_{0,\mathrm{off}}$	10.3 cm s^{-1}
Wave orbital semiexcursion, $A_0 = u_0 T/2\pi$	3.8 cm
Water depth, h	31 cm
Wave asymmetry, As	0.58
Wave skewness, Sk	0.12
Kinematic viscosity of water, ν	1.004×10^{-6} m^2 s^{-1}
Sediment median grain diameter, d_{50}	0.54 mm
Sediment specific gravity, $s = \rho_p/\rho$	1.2
Sediment settling velocity, w_0	1.8 cm s^{-1}
Ripple height, η_b	0.8–1 cm
Ripple wavelength, λ_b	4.5–7 cm
Migration rate, c_b	−0.005 cm s^{-1}
Reynolds number, $\mathrm{Re} = u_0^2 T/2\pi\nu$	4400
Particle Reynolds number, $\mathrm{Re}_s = w_0 d_{50}/\nu$	9.7
Stokes number, $\mathrm{Stk} = \pi d_{50}^2 s/9\nu T$	0.06
Wave friction factor, $f_{2.5} = \exp\left[5.213(2.5d_{50}/A_0)^{0.194} - 5.977\right]$	0.039
Grain roughness Shields parameter, $\theta_{2.5} = f_{2.5} u_0^2/2(s-1)gd_{50}$	0.26
Sleath parameter, $S = 2\pi u_0/(s-1)gT$	0.19
Kolmogorov length scale, $l_K \sim \eta_b \mathrm{Re}^{-3/4}$	O (0.01) mm
Kolmogorov velocity scale, $u_K \sim u_0 \mathrm{Re}^{-1/4}$	O (1) cm s^{-1}
Kolmogorov time scale, $t_K \sim l_K/u_K$	O (0.001) s

described in *Van den Boomgaard* [2003]). The coordinate system of this study defines x positive offshore, z positive upward, and y positive out-of-the-paper.

[8] Correct physical modeling of the nearshore sediment transport in a laboratory setting requires significant scaling of the sediment particles. In order to preserve the Froude number, particle Reynolds number, Shields parameter and relative settling velocity for these wave characteristics, a sediment specific gravity (s) of 1.2, and median grain diameter (d_{50}) of 0.54 mm was necessary [*Henriquez et al*., 2008]. These sediment characteristics produced a grain roughness Shields parameter of 0.26, a particle Reynolds number of 9.7, and ripples of approximately 1 cm in height and 5 cm in wavelength, for the prescribed wave conditions (Table 1). Self similar field conditions would include quartz sediment grains with $d_{50} = 0.22$ mm and $s = 2.65$, and waves 50 cm in height, 6 s in wave period in 3 m of water depth.

[9] A Shields parameter of 0.26 would result in a local morphology squarely within the ripple regime and consistent with the observed bed forms. However, for the case of this scaled sediment, the horizontal pressure gradient may also contribute to the sediment dynamics. Bed dilation and subsequent plug flow conditions occur when the ratio of wave-induced pressure gradients to the immerse weight of the grains, the Sleath parameter, exceeds 0.29 according to the oscillatory laboratory studies by *Sleath* [1999], or 0.1 according to field observations by *Foster et al*. [2006]. The wave forcing conditions in this effort yielded a Sleath parameter of 0.19 (Table 1), which suggests pressure gradients may contribute to the sediment dynamics. Ancillary support for the possible influence of the pressure gradient in these conditions was provided by visual observations of a persistently thick ($\sim$10 grain diameters) mobile layer in this dynamic rippled bed. However, *Henriquez et al*. [2008] conclude that the mobility of the sediment bed may be larger than expected due to the scaling effects associated with a mismatch in the Sleath parameter.

2.2. Velocity Measurements

[10] A Dantec particle image velocimetry (PIV) system resolved the 2-D velocity field and ripple profile (Figure 1). The free-stream velocity was measured with an acoustic Doppler velocimeter (ADV), time-synchronized with the PIV. The PIV system consisted of a 120 mJ ND:YAG laser vertically located 27 cm above the bed, illuminating a vertical (x-z) slice of the water column. In contrast to previous efforts [*Nichols and Foster*, 2007], the laser was operated in low power mode, to reduce bed reflections (Figure 2a). A 1 megapixel camera (1016 pixels $\times$ 1008 pixels) located outside the wave flume obtained image pairs over a 11 cm $\times$ 11 cm sampling window at 12 Hz for 60 s bursts, leading to a total of 720 velocity fields (30 waves in each burst). The time between image pair members was selected as 10 ms to prevent particles from moving more than one third of a correlation window (21 pixels, 2.3 mm). Seeding material included sediment particles, microbubbles, and organic matter.

[11] Velocity vectors were calculated using, MatPIV 1.6.1, developed by *Sveen* [2004]. Correlations were calculated with two passes with interrogation windows of size 64 pixels in the horizontal and 32 pixels in the vertical, with 50% overlap. Because velocity vectors result from the average particle displacement within each correlation window, rectangular windows were employed to decrease the effect of vertical velocity gradients on the Reynolds stress and other estimated quantities, while increasing their vertical resolution. This approach was justified by the magnitude difference between the horizontal and vertical velocity components (u and w, respectively), with particles traveling about 10 times the distance in x than in z. The spatial resolution of the resulting velocity field is 3.5 mm in the

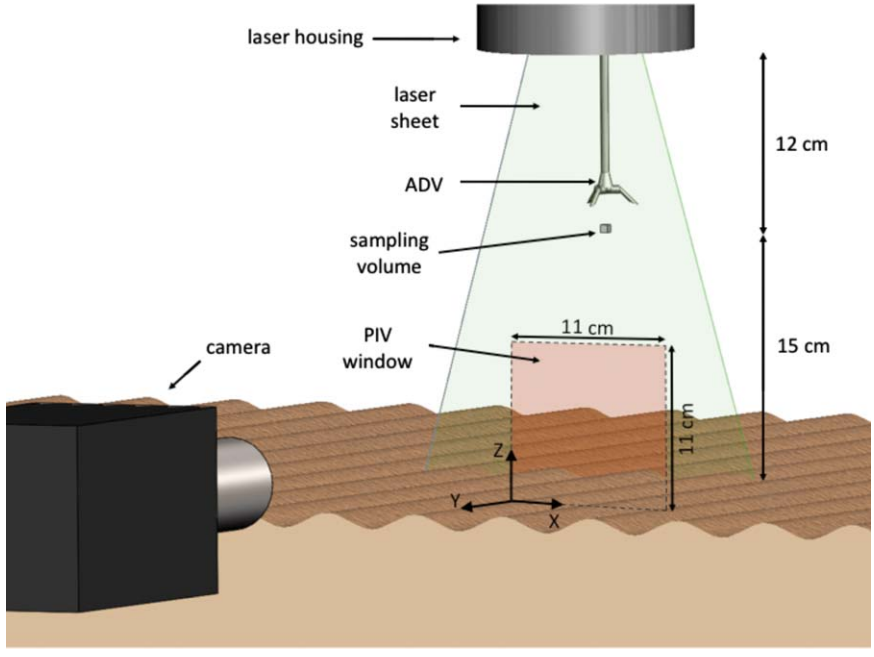

Figure 1. Schematic diagram of the laboratory setup and PIV observation window.

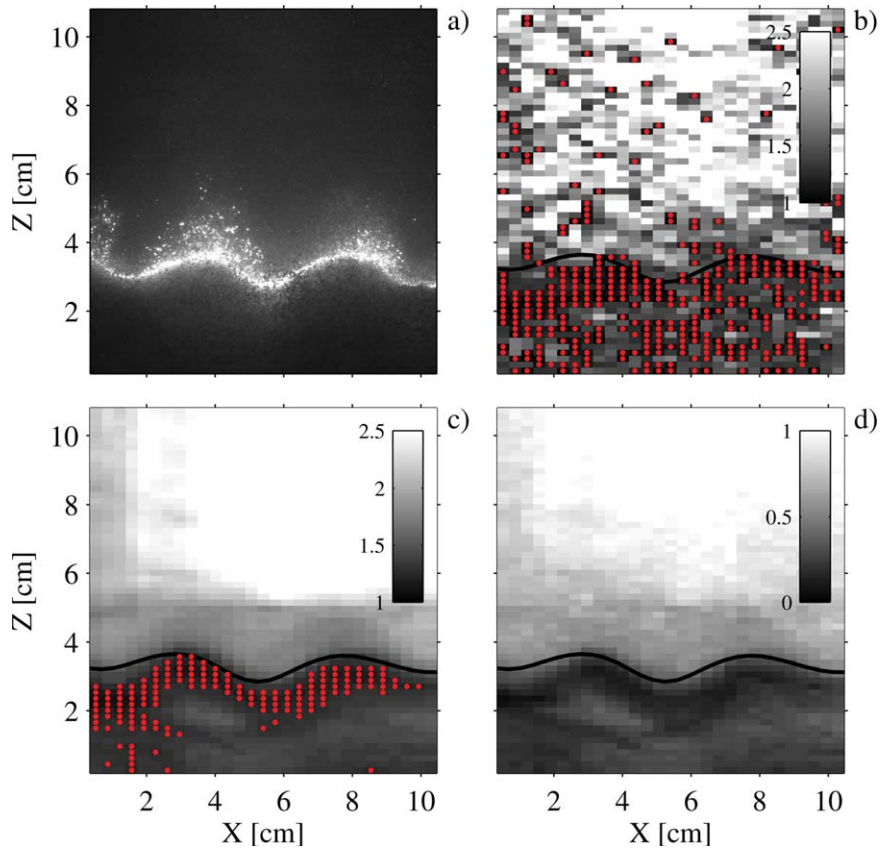

Figure 2. (a) Instantaneous PIV image. (b) Ratio of the highest PIV correlation peak to the second highest (dimensionless) for the instantaneous image shown in Figure 2a. (c) Time-average and (d) standard deviation of the ratio of the highest to second highest peak over the entire 60 s realization. Time-averaged bed estimates are shown by the black solid lines. Ratios corresponding to a value <1.2 are shown in red.

horizontal and 1.7 mm in the vertical. Particle displacements were calculated at the subpixel level using a three-point Gaussian estimator [*Raffel et al*., 2007].

[12] Noise resulting from unrealistic velocity estimates associated with the PIV technique was reduced with a three standard deviation filter. The total number of spurious vectors detected corresponded to less than 3.5% of the observations, for both u and w. After detection, outliers were replaced with the local phase average defined as

$$\tilde{q}(\tilde{t}) = \frac{1}{M}\sum_{m=0}^{M} q(t + mT), \tag{1}$$

where $\tilde{q}$ represents any phase-averaged flow quantity, $\tilde{t}$ is the phase, $M = 30$ is the total number of waves, and $T = 2$ s is the wave period.

[13] The free-stream velocity vectors were validated with point measurements provided by the ADV following *Nichols and Foster* [2007]. The uncertainty level of the horizontal velocity was computed following *Cowen et al*. [2003] and *Nichols and Foster* [2007], with a bootstrap analysis at the 95% significance level [*Efron and Tibshirani*, 1993]. Taking the ADV time series as the true value, and the filtered PIV time series at $x = 5.23$ cm and $z = 9.24$ cm, resulted in an uncertainty of ± 0.72 cm s^{-1} ($\pm 6\%$ the horizontal velocity amplitude, u_0). Please note that this estimate also includes any uncertainty related to the ADV measurements.

[14] Closer to the bed, velocity gradients, bed reflections, and sediment suspensions may influence PIV displacement calculations. The effects of bed reflections and velocity gradients were reduced by lowering the power of the laser (Figure 2a), and using rectangular interrogation windows, respectively. Their potential influence on the PIV velocity estimates is depicted by the ratio of the highest to second highest correlation peak in each interrogation window. Generally, correlation peaks used to calculate displacements were influenced by their proximity to the bed (Figures 2b–2d). However, on average, they still met the 1.2 threshold proposed by *Keane and Adrian* [1992], and previously used by *van der A et al*. [2011]. Nevertheless, care must be taken when interpreting the results of the first cell above the bed estimate, where strongest reflections and sharpest velocity gradients occur.

[15] The size and number of particles in an interrogation window is strongly related to the accuracy of the final velocity measurement [*Dong et al*., 1992; *Huang et al*., 1999]. Near the bed, the 0.54 mm sediment particles corresponded roughly to a 5×5 pixel trace size, with an average of 20 particles per interrogation window, including other seeding material. However, coherent sediment plumes

(further discussed later in the paper) resulted in a variability of ± 10 particles near the crests of the ripples. The trace size and number of particles allow for a conservative uncertainty estimate of 0.3 pixels, based on previous efforts by *Bertuccioli et al*. [1999] and *Nimmo Smith et al*. [2005]. With an expected displacement of 12 pixels during peak flows, the corresponding uncertainty is 2.5%. For the case of the Reynolds stress estimate, the uncertainity improves with the square root of the total number of points averaged (i.e., $\sqrt{720}$), but increases by one order of magnitude for differential quantities, such as $\mu \frac{\partial u}{\partial z}$ [*Nimmo Smith et al*., 2005].

[16] The settling velocity of the bed sediment was estimated to be 1.8 cm s^{-1}, following *Cheng* [2009]. The corresponding wave-based Stokes number was 0.06 (Table 1) and, therefore, particles were assumed to follow the wave-induced motions closely $(\mathrm{Stk} << 1)$. However, the relatively large size of the bed sediment particles prevented resolution of the smallest scales of turbulence ($l_K \sim$ O(0.01) mm, $u_K \sim$ O(1) cm s^{-1}, $t_K \sim$ O(0.001) s, Table 1. In this investigation, we will focus the analysis on integral flow quantities, rather than the turbulence microscales.

[17] As the PIV laser sheet illuminated both bed sediment suspended in the water column and other smaller particles with substantially less settling potential (sediment fragments, organic matter, etc.), the effect of sediment settling velocity on the PIV measurements was expected to be minimal and, therefore, no settling was subtracted from the vertical velocity signal. The same argument yields to the assumption of minimal settling-induced turbulence, and therefore negligible trajectory bias [*Maxey*, 1987].

[18] Similar efforts that have successfully achieved near-bed PIV velocity measurements with strong presence of loose sediments and/or spatial nonuniformity in particle concentration, include those of *Ahmed and Sato* [2001], *Nichols and Foster* [2007], *Van der Werf et al*. [2007], and *van der A et al*. [2011].

2.3. Bed Elevation

[19] Previous optical and acoustic studies have approximated the bed position to generally within 1 cm [*Crawford and Hay*, 2001; *Doucette and O'Donoghue*, 2006a; *Van der Werf et al*., 2007; *Nichols and Foster*, 2007, 2009]. However, they either rely on sonar scanning times that are long compared to the wave period [*Doucette and O'Donoghue*, 2006a], laser point measurements during inactive flow conditions [*Van der Werf et al*., 2007], or time averages of image intensity over entire data realizations [*Nichols and Foster*, 2007, 2009]. In the latter, bed reflections associated with the PIV laser sheet presented serious difficulties within the lowest 1 cm from the bed. In this study, we will follow the method of *Nichols and Foster* [2007], replacing the time-averaged image with the phase average defined with equation (1). Image phase averaging is a valid approach for determining bed elevations in this data set, as the total migration of the ripples is considerably slow (0.005 cm s^{-1}) compared to the duration of the realization (60 s). Bed elevation estimates from phase-averaged pixel images were contaminated by recurrent coherent sediment plumes obscuring the bed (Figure 3b). In this effort, the effect of the coherent plumes was eliminated by using the phase-maximum pixel intensity ($I_{\max}(x, z, \tilde{t})$, Figure 3a) as the bed elevation baseline. The phase-maximum pixel intensity is defined with

$$I_{\max}(x, z, \tilde{t}) = \max(I(x, z, t + mT), \forall\ m = 0, 1, 2, ..., M - 1), \tag{2}$$

where I is the intensity value in each pixel and $M = 30$ is the total number of waves. A bed position baseline, $z_{\mathrm{base}}(x, \tilde{t})$, is taken as the lowest-elevation point with the maximum pixel intensity in the phase-maximum pixel image (Figure 3a). The actual bed position, $z_b(x, \tilde{t})$, is assumed to be the baseline estimate plus a constant given by

$$C(\tilde{t}) = \langle z_c(x, \tilde{t}) - z_{\mathrm{base}}(x, \tilde{t}) \rangle, \tag{3}$$

where the angle brackets represent spatial average in the x direction and z_c is the centroid of the phase-averaged pixel image as suggested by *Nichols and Foster* [2007]. The final bed height is given by

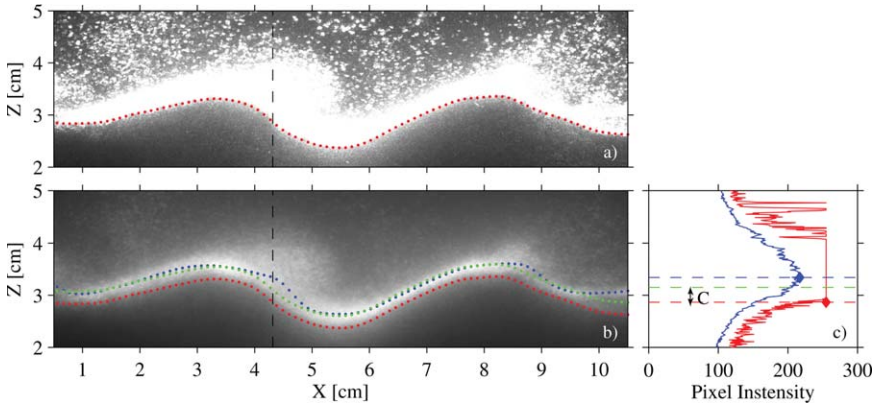

Figure 3. (a) Phase-maximum and (b) phase-averaged pixel image at $\tilde{t} = 235°$ showing: z_{base} (red), z_c (blue), and z_b (green). (c) Vertical profiles of phase-maximum (red) and phase-averaged (blue) pixel intensity at $x = 4.32$ cm with diamonds corresponding to the values in Figures 3a and 3b as shown by the black dashed line. Images have been zoomed into the near-bed region.

$$z_b(x,\tilde{t}) = z_{\text{base}}(x,\tilde{t}) + C(\tilde{t}). \quad (4)$$

Finally, a running average of size 30 pixels (3.2 mm) was applied to z_b.

[20] The variability of z_b over $\tilde{t}$ fluctuated between 2 mm at the trough and 6 mm at the onshore slope of the rightmost ripple. This approach is different form that used by *Nichols and Foster* [2007] by a root-mean-square difference of ~2 mm, computed by comparing the centroid of the mean intensity image over the 720 samples to the mean bed elevation found by averaging the 24 phases. As z_b is resolved at 1 pixel resolution, velocity measurements corresponding to interrogation windows at or below z_b were excluded (masked) from the analysis.

2.4. Wave Characteristics

[21] Figure 4a shows that skewed and asymmetric waves, characterized by longer offshore-directed half-wave periods (positive horizontal velocity with lower peak magnitudes) and shorter onshore-directed half-wave periods (negative horizontal velocity with higher peak magnitudes), were present at the instrument location. The wave skewness (Sk = 0.12) and asymmetry (As = 0.58) were estimated using the free-stream ($x = 5.23$ cm, $z = 9.24$ cm) velocity skewness and temporal asymmetry, respectively, following *Gonzalez-Rodriguez and Madsen* [2007]. Based on the work by *Elfrink et al*. [2006], these wave characteristics will be present in field conditions with a constant bed slope of 1:20 and $Hh^{-1} \approx 0.2$ and $\lambda h^{-1} \approx 10$.

[22] Positively asymmetric waves have a forward leaning face and a gentle rear, which induces highest fluid accelerations in the onshore direction. The implications include higher bed shear stresses, and consequently higher sediment pick up rates, during the onshore half-wave period [*Nielsen*, 2006; *Gonzalez-Rodriguez and Madsen*, 2007]. Wave skewness results from the evolution of the wave field

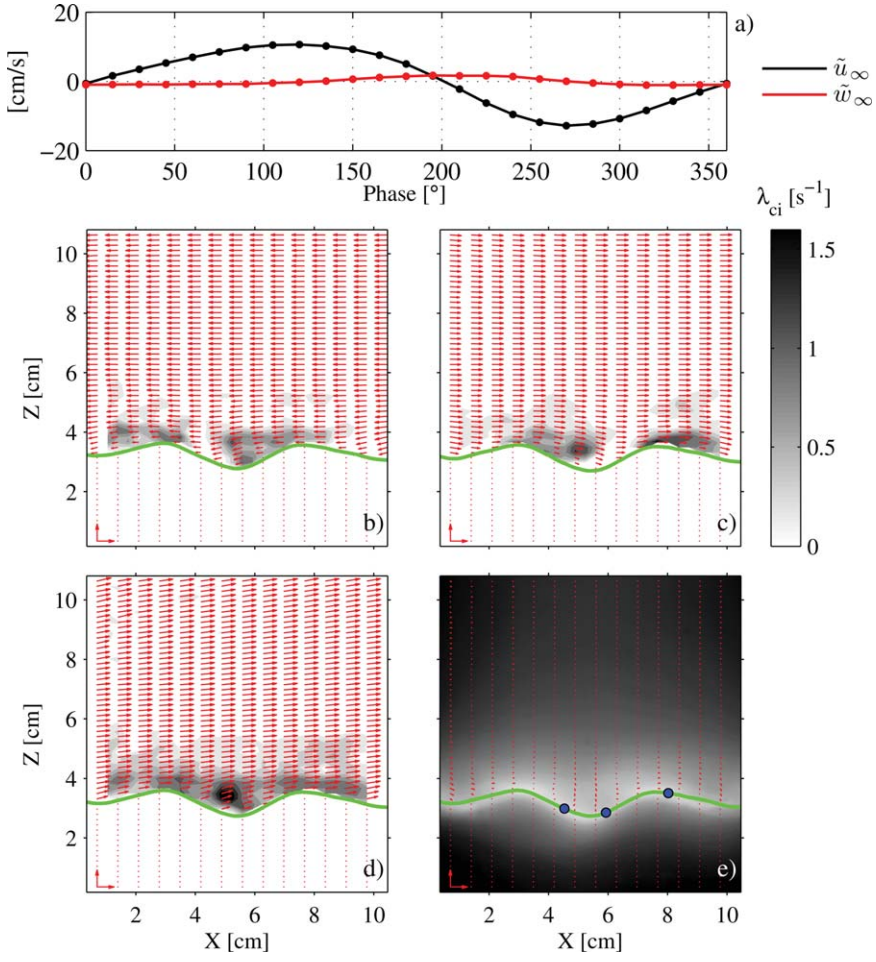

Figure 4. (a) Free-stream horizontal (black) and vertical (red) velocity for one wave period at $x = 5.23$ cm and $z = 9.24$ cm. (b) Onshore-averaged flow and (c) offshore-averaged flow (red vectors) over the corresponding half-wave averaged swirling strength (λ_{ci}), as shown by the gray colormap. (d) Standard deviation velocity field (red vectors) over the rms λ_{ci} (gray colormap). (e) Mean velocity field (red vectors) over the mean image intensity computed over the 60 s PIV realization. Scale vectors represent 10 cm s^{-1}. Velocity data under z_b (green solid line) have been masked. Onshore flow is directed to the left. Blue dots on Figure 4e provide the horizontal location for the data presented in Figure 5.

along the tank and is consistent with shoaling of ocean waves [*Elgar and Guza*, 1985]. Narrow crests and wide troughs result in longer excursion times in the offshore direction, and the potential for offshore sediment transport [*Hassan and Ribberink*, 2005]. We can anticipate that these nonlinearities in the wave field will affect the boundary layer dynamics [*van der A et al*., 2011] and bed form evolution [*Crawford and Hay*, 2001].

3. First-Moment and Second-Moment Velocity Statistics

[23] Approximations of various hydrodynamic- and sediment transport-related characteristics are evaluated with both the first and second moments of the regular monochromatic wave observations. The first moment of the velocity field is defined with the time-average of the velocity field over half-wave periods, which were detected by finding the zero-crossings in the horizontal free-stream velocity. Half-wave periods in each horizontal flow direction (onshore and offshore) were averaged over an entire realization, resulting in a mean velocity field for each flow direction, consisting of u_{on} (x, z) and w_{on} (x, z) in the onshore (x negative) direction and u_{off} (x, z) and w_{off} (x, z) in the offshore (x positive) direction (Figures 4b and 4c).

[24] The second moment of the velocity field is defined with the square root of the variance (i.e., the standard deviation) of the horizontal and vertical velocity components, u_{std} (x, z) and w_{std} (x, z) (Figure 4d). Standard deviation velocity estimates are common in the literature [*Cox et al*., 1994; *Trowbridge and Lentz*, 1998; S*haw and Trowbridge*, 2001] as they allow for simple assessment of the magnitude of the wave field.

[25] The slightly skewed and asymmetric wave forcing and the presence of a rippled boundary induce a complex flow pattern, characterized be shedding vortices and a "jet regime" [*Gimenez-Curto and Corniero Lera*, 1996] above the ripple crests. While this paper will focus the analysis on boundary layer characteristics and flow quantities derived from first-moment and second-moment velocity statistics, we understand that a brief temporal and spectral description of the flow within the WBBL is in order, before furthering the quasi-steady analysis.

4. Temporal Variability

[26] Inflection points in the vertical profiles of the phase-averaged horizontal velocity near the central trough of the ripples ($x = 4.5$ and 5.9 cm, Figures 5a and 5c, respectively) provide evidence of boundary layer separation during phases of flow reversal (roughly 0° and 180°). The separated boundary induces a phase lag that is evident at elevations roughly between 4 and 5 cm, and a phase lead confined to elevations below 4 cm. Phase separation will be further discussed in section 5.

[27] Sharp transitions in the velocity profiles near the ripple trough are more evident during peak flows above lee slopes (Figures 5a and 5c), that is, peak offshore ($\tilde{t} = 120°$) at $x = 4.5$ cm and peak onshore ($\tilde{t} = 270°$) at $x = 5.9$ cm. Although we cannot suggest a physical reason for these slope discontinuities other than experimental noise, their occurrence suggests a dependence on boundary geometry given perhaps by the adverse pressure gradients at the lee slopes. Clear signatures of velocity overshoot, typical in oscillating boundary layers and explained with the velocity defect acting as a "dampened wave" propagating from the boundary [*Nielsen*, 1992], are observed during peak offshore flow, at the rightmost ripple crest ($x = 8$ cm, Figure 5e). Velocity profiles during peak flows at this location also suggest a slipping boundary.

[28] This temporal and vertical complexity in the nearbed velocity may be a result of periodic "jets" associated with the vortical structures generated by the large-scale boundary irregularities, as previously suggested by *Sleath* [1987] and *Gimenez-Curto and Corniero Lera* [1996]. Following *Zhou et al*. [1999] and *Nichols and Foster* [2007], coherent flow structures were identified with the swirling strength criterion (λ_{ci}) computed from phase-averaged horizontal and vertical velocities. Half-wave averages of λ_{ci} (Figures 4b and 4c) are consistent with swirling motions generated at the ripple crests and prevailing over the lee slope of the ripples. The strongest signatures are present for the offshore half-wave period, and may be explained by the temporal asymmetry and velocity skewness characterizing the wave field. The rms swirling strength (Figure 4d) show two distinct layers separated at roughly $z = 4$ cm. Consistent with qualitative observations of the phase-averaged pixel intensity provided in *Rodriguez-Abudo* [2011], and previous observations by *Van der Werf et al*. [2007], the weak swirling signatures above $z = 4$ cm, may be related to vortices generated by adjacent ripple crests, which have been shed into the water column and advected into the flow with a slight lost of strength.

5. Spectral Variability

[29] Stacks of horizontal velocity spectra for three different horizontal locations (Figures 5b, 5d, and 5f) clearly show adequate resolution throughout the water column of the incident wave band and the next harmonic. Consistent with the ratio of the highest to second highest PIV correlation peaks (Figure 2), the noise floor increases generally from right to left in the image, and from top to bottom.

[30] To further explore the space-dependent spectral decay/enhancement of the horizontal velocity, the power spectral density and corresponding phase separation at the incident wave band (f_0) and two higher harmonics ($2f_0$ and $3f_0$) with respect to the free stream are presented in Figure 6. The energy at the incident band shows an amplitude decay of roughly 80% in the immediate proximity to the bed (Figure 6a). In a laboratory study concerning the spectral decay of surface gravity waves, *Doering and Baryla* [2002] observed an amplitude decay of roughly 50% just outside the boundary layer under Stokes waves over a rippled sediment bed.

[31] The local phase separation was computed from cross-spectral analysis against the spatially averaged free-stream velocity. Space- and time-dependent horizontal velocity, u (x, z, t), was compared against the corresponding free-stream velocity, u_∞ (x, t). Consistent with Figure 5e, phase leads are present roughly η_b above the crest. Since waves propagate from right to left, there is a slight phase lead at the offshore side of the image, and a phase lag at the onshore side. Generally, the boundary layer leads the free

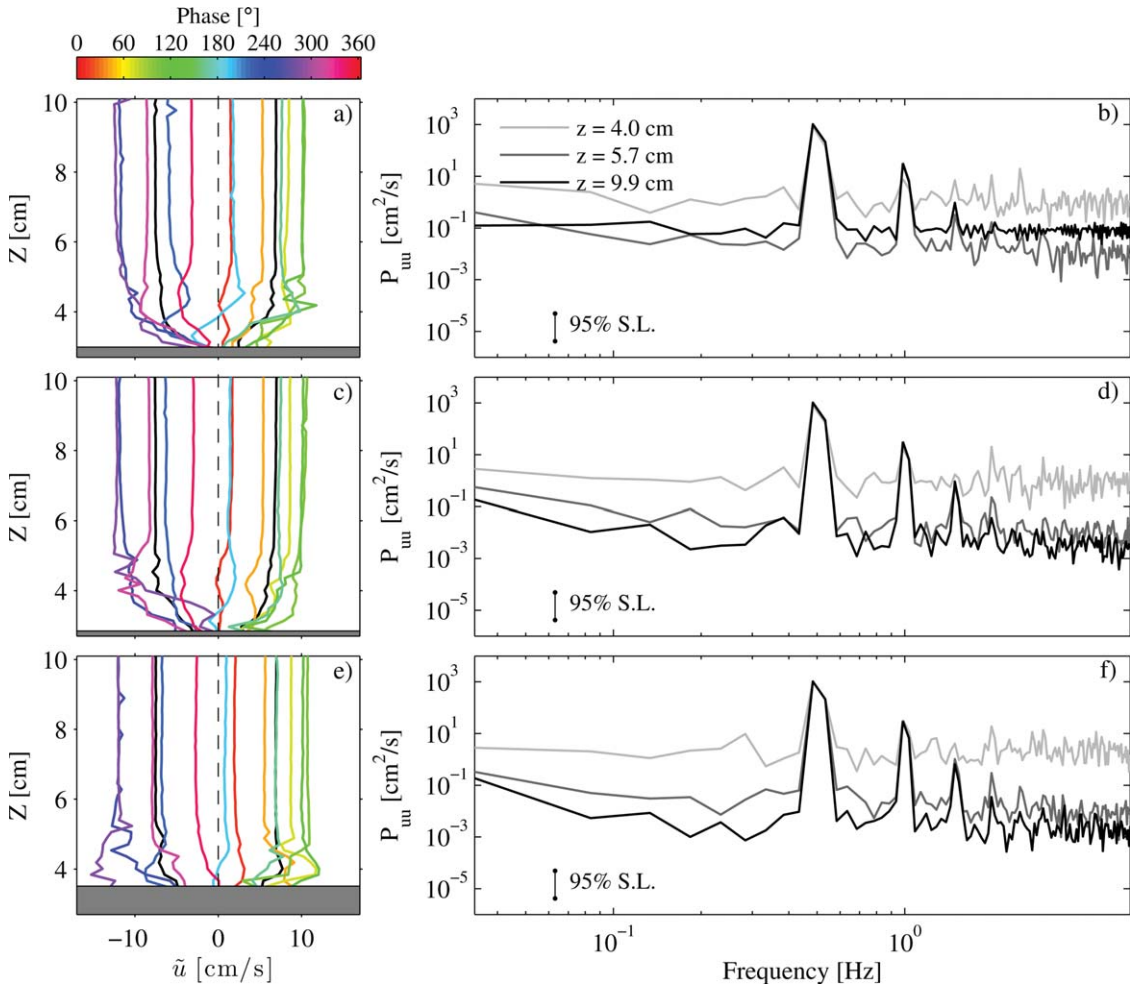

Figure 5. (a, c, e) Vertical profiles of ensemble-averaged horizontal velocity ($\tilde{u}$) at $x = 4.5$, 5.9, and 8 cm, respectively, for wave phases indicated by the colorbar. For clarity, only every other wave phase is shown. Onshore and offshore half-period averages are shown in black. (b, d, f) Power spectral density of u at various elevations along a vertical slice located at $x = 4.5$, 5.9, and 8 cm, respectively. Significance levels were calculated with 6 degrees of freedom.

stream by 0–25°. These values show variability over the ripple, but are greater than previous observations of the WBBL over flat beds, which showed roughly 10° phase lead [*Trowbridge and Agrawal*, 1995; *Foster et al*., 2000]. Note that the near-bed phase lead at the central trough ($x = 5.1$ cm) is not as high as at the other troughs ($x = 0.5$ cm and $x = 10.2$ cm), likely due to stronger adverse pressure gradients present in this relatively deeper ripple trough. Higher in the water column, a phase lag of 10° is observed above the main ripple trough, showing consistency with Figures 5a and 5c. This lag is suggestive of vortices being shed from the ripples during flow reversals and is not inconsistent with the rms swirling strength presented in Figure 4d.

[32] At the first harmonic ($2f_0$), the spectral energy amplitude is lower than at the incident band (f_0) and decreases near the bed (95% decay). A strong phase lead of roughly 100° is observed at the main ripple trough (Figure 6e), and may be suggestive of the role of horizontal pressure gradients in this relatively deeper trough. Free-stream spectral energy at the second harmonic ($3f_0$) is about 5% of the energy contained in the first harmonic ($2f_0$). However, a statistically significant increase of almost two orders of magnitude is observed with proximity to the bed (order 1 and 100 given by the colors cyan and yellow, respectively, in Figure 6c and top colorbar). The strong amplification of spectral energy in the near-bed region suggests that not only the nonlinearities imposed by the skewed wave field play a role within the boundary layer [*van der A et al*., 2011], but also that these are highly amplified due to presence of a rippled boundary. This is consistent with numerical [*Ning et al*., 2012] and experimental [*Beji and Battjes*, 1993] studies showing increasing amplitude in the higher harmonics of a wave field at the lee side of large-scale bars in the nearshore.

[33] Slight phase leads (30°) at the second harmonic ($3f_0$) are visible at the left and right ripple troughs (Figure 6f). Contrastingly, at the main ripple trough, a strong phase separation (±180°) with respect to the free stream is observed at the ripple slopes. As a matter of fact, in their study over flat sand beds, *van der A et al*. [2011] saw the strongest phase separation occurring at the second harmonic. They also found that almost perfectly sinusoidal flows, like the one in the present study, are more susceptible to strong

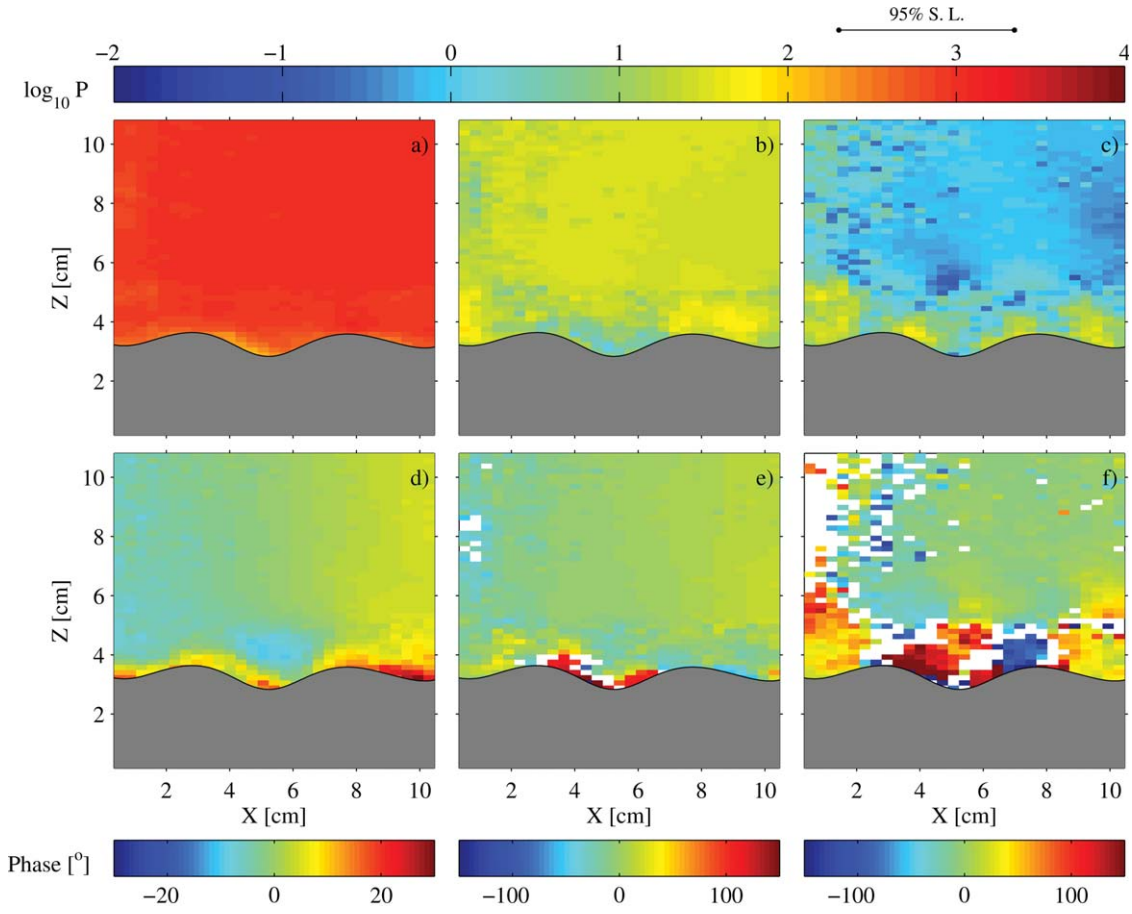

Figure 6. Spectral energy of u (upper row) and phase separation between u and u_∞ (lower row) for (a, d) the incident band [$f_0 = 0.5$ Hz], (b, e) the first harmonic [$2f_0 = 1$ Hz], and (c, f) the second harmonic [$3f_0 = 1.5$ Hz]. Phase separation data are only shown for coherence exceeding the 95% significance level with 6 degrees of freedom.

phase separations at the second harmonic than are highly acceleration skewed flows. For the present study, we expect the asymmetry in the rippled bed, provided by the deeper ripple trough, to further increase the phase separation due to the adverse and favorable pressure gradients imposed by each ripple slopes. Once again, these findings suggest that nonlinearities in the wave field and ripple geometry may play an important role in the characterization of the near-bed turbulent flow and boundary layer thickness. In general, Figure 6 suggests that above $z \approx 5$ cm, the spectral characteristics are uniform, and the boundary layer is confined to $\sim$2 cm at the troughs, and $\sim$1 cm at the crests.

6. Boundary Layer Thickness

[34] The thickness of the boundary layer was also characterized for first-moment and second-moment statistics with an integral approach for the displacement and momentum thicknesses. The displacement thickness, δ^*, is the distance the bed will be upwardly displaced in a frictionless flow so as to maintain the same mass flux [*Schlichting*, 1979]:

$$\delta^*(x) = \int_{z_b}^{\infty} \left(1 - \frac{u(x,z)}{u_\infty(x)}\right) \mathrm{d}z. \tag{5}$$

[35] Figure 7 shows δ^* for first-moment (onshore and offshore) and second-moment (standard deviation) flow statistics. Consistent with laminar boundary layers, δ^* becomes thicker in response to the adverse pressure gradient present in the ripple trough. The increased thickness is also consistent with the expanded logarithmic layers shown in Figure 8. Moreover, the smaller boundary layer thicknesses at the ripple crests are expected due to flow acceleration and are particularly evident in Figure 7e. Flow amplification at the ripple crest may result in enhanced shear [*Nielsen*, 1986], and induce a slip boundary. The relationship between the shear stress and the bottom boundary will be further discussed later in the paper.

[36] The momentum thickness, δ_{mom}, represents the distance the bed would be displaced upward in an inviscid flow in order to conserve the same momentum deficit:

$$\delta_{\mathrm{mom}}(x) = \int_{z_b}^{\infty} \frac{u(x,z)}{u_\infty(x)} \left(1 - \frac{u(x,z)}{u_\infty(x)}\right) \mathrm{d}z, \tag{6}$$

[37] Figure 7 shows that δ_{mom} and δ^* behave similarly, although the magnitudes of δ_{mom} are slightly lower than δ^*, especially above ripple troughs. The ratio of δ^* to δ_{mom} provides information regarding flow separation in turbulent flows [*White*, 1994]. Large ratios imply a momentum loss

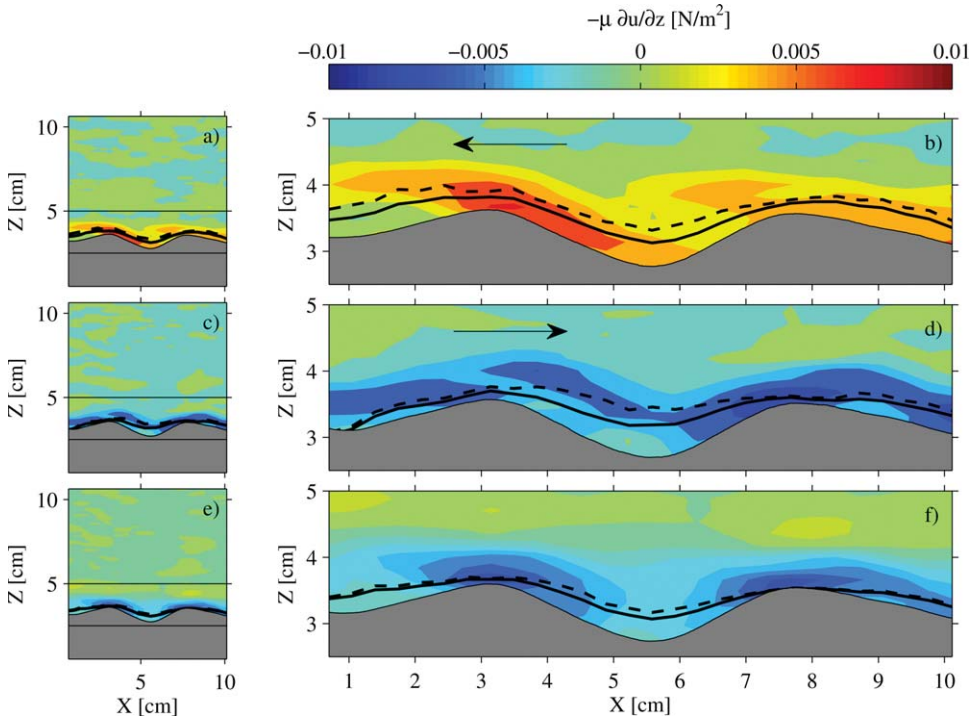

Figure 7. Viscous shear stress (color scale) in the nearbed region (right column) and over the entire imaged area (left column) as calculated with u_{on} (x, z) (a, b), u_{off} (x, z) (c, d), and u_{std} (x, z) (e, f), with corresponding bed elevation (gray), for a single realization. Data under z_b have been masked. The displacement thickness, δ^*, and momentum thickness, δ_{mom}, are indicated by the black dashed and solid lines, respectively. Black arrows indicate the direction of the flow.

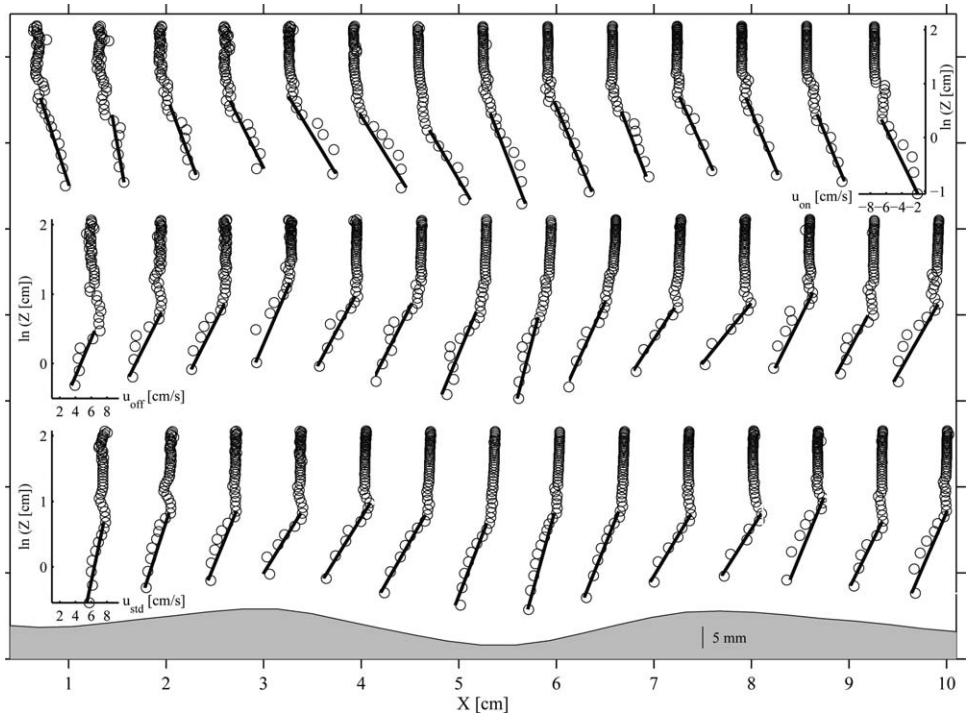

Figure 8. Horizontal velocity profiles (open circles) plotted on a logarithmic scale at every second horizontal location for (top) onshore-directed flow, (center) offshore-directed flow, and (bottom) standard deviation. The least-squares fit to the horizontal velocity profiles is plotted with a black solid line. The mean bed elevation is shown in gray.

near the boundary in response to adverse pressure gradients inducing flow separation. This is evident in Figures 7a and 7b, as flow constricts up the ripples' stoss slopes and crests maintaining a low $\delta^*/\delta_{\mathrm{mom}}$ ratio, and then diverges at the lee slopes and troughs with higher $\delta^*/\delta_{\mathrm{mom}}$ ratios. This is not as evident for the standard deviation estimates, although $\delta^*/\delta_{\mathrm{mom}}$ remains high at the center ripple trough.

[38] As shown in Table 2, the integral approach for estimating boundary layer thickness using δ^* and δ_{mom} yields results that are almost four times smaller than boundary layer thicknesses suggested by the decay of the higher harmonics (O(1–2) cm), although their relationship may be more complex. It should be noted that the integral approach becomes problematic when velocity overshoots or streamlines narrow above the ripple crests, resulting in $u > u_\infty$, and negative values of δ^*, as seen in Figure 7b for $x < 1$ cm, and Figure 7c at the rightmost ripple crest ($x = 8$ cm).

7. Viscous Stress

[39] Also shown in Figure 7 is the viscous shear stress ($-\mu\frac{\partial u}{\partial z}$, where μ is the dynamic viscosity of water). In turbulent flows, the viscous shear should be several orders of magnitude less than the total shear, however, it provides a qualitative notion of the flow behavior. Viscous shear is larger on the stoss side of the ripples for both onshore directed and offshore directed flows. This is also consistent with flow acceleration as it constricts up the ripple face. Conversely, the flow decelerates on the lee side of the ripple, forming a wake-like area that remains present until it is affected by the presence of the next ripple [*Nelson and Smith*, 1989; *Wiberg and Nelson*, 1992; *Li*, 1994; *Coleman et al*., 2008]. This suggests the presence of a recirculating area after the ripple crest, in a manner analogous to a backward facing step [*Nichols and Foster*, 2007], and consistent with the average swirling strength signal (Figures 4b and 4c).

[40] The magnitude of the viscous shear is higher during the offshore directed flow. This is opposite to the onshore directed bed form migration, suggesting that higher order terms may be responsible for ripple mobilization, such as skewness of the near-bed orbital velocity [*Crawford and Hay*, 2001], and vortex formation and ejection [*Traykovski et al*., 1999]. During the strong onshore directed flow (Figure 7a), high shear is generated at the stoss side of the ripple ($x = 3-4.5$ cm), where the pressure gradient is favorable, and then shed into the water column forming a wake-like region, with little to no viscous shear at the lee side. This is less evident for the offshore directed flow (Figure 7a), where viscous shear appears to follow the geometry of the bed more closely, probably due to the milder free-stream flow and longer excursion times. The longer excursion times allow for increased boundary layer development. In the standard deviation case, the viscous shear goes to zero at heights below 4.5 cm regardless of location along the ripple, and the sharpest gradients occur at the offshore ripple slopes and crests, suggesting a strong dependence on the dynamics present during the onshore directed flow. Each of the three cases show qualitatively that the region where velocity gradients are considerable is comparable to boundary layer thickness estimates using the higher harmonics (O(1–2) cm).

8. Shear Velocity and Roughness Estimates

[41] Horizontal velocity profiles across the rippled bed for the onshore, offshore, and standard deviation flows are presented in Figure 8. Although the shape of the velocity profiles is affected by vortex shedding, and the logarithmic law may not be valid in this complex environment, Figure 8 suggests that the first and second moments of the horizontal velocity generally decay logarithmically.

[42] In his study concerning atmospheric boundary layers over a urban canopy, *Jackson* [1981] showed that velocity profiles above large roughness elements follow a logarithmic law of the form

$$u = \frac{u_*}{\kappa}\ln\left(\frac{z - d_*}{z_0}\right), \tag{7}$$

where u_* is the shear velocity, $\kappa = 0.4$ is the Von Karman coefficient, z_0 is the hypothetical vertical position where $u = 0$, and d_* is the displacement height. *Jackson* [1981] showed that d_* represents the average level at which the mean drag appears to act on a rough boundary. In the case of a rippled boundary, d_* may be associated with the manifestation of the flow blockage introduced by the ripple crest, and therefore dependent on the ripple size and shape.

[43] Iterative methods are commonly used to find d_* in studies where the lowest velocity measurement is taken just above the tallest roughness element [*Cox et al*., 1996]. The spatial resolution in this effort allows us to obtain velocity observations between the roughness elements, and therefore examine the spatially variable displacement height

Table 2. Overall Spatially Averaged Results for the Four Realizations With Corresponding Standard Deviation

Parameter	Units	Onshore	Offshore	Standard Deviation
δ^*	[cm]	0.57 ± 0.22	0.30 ± 0.21	0.28 ± 0.16
δ_{mom}	[cm]	0.40 ± 0.14	0.21 ± 0.13	0.22 ± 0.12
Δz	[cm]	0.42 ± 0.17	0.44 ± 0.20	0.38 ± 0.15
d_*	[cm]	2.34 ± 0.39	2.31 ± 0.42	2.35 ± 0.38
u_*	[cm s^{-1}]	-1.42 ± 0.43	1.23 ± 0.40	1.04 ± 0.29
θ_{u_*}	[–]	0.21 ± 0.13	0.17 ± 0.11	0.11 ± 0.06
z_0	[cm]	$0.23 \le 0.31 \le 0.38$	$0.20 \le 0.27 \le 0.33$	$0.07 \le 0.11 \le 0.15$
R	[cm]	$7.0 \le 9.2 \le 11.3$	$5.9 \le 8.0 \le 9.9$	$2.2 \le 3.2 \le 4.4$
z_{base}	[cm]	2.76 ± 0.29	2.75 ± 0.29	2.73 ± 0.29
min (z_{base})	[cm]	2.27 ± 0.08	2.25 ± 0.09	2.23 ± 0.08
max (z_{base})	[cm]	3.25 ± 0.13	3.25 ± 0.12	3.23 ± 0.13

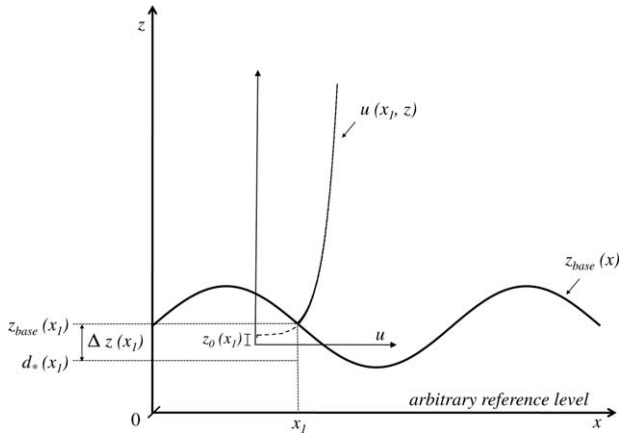

Figure 9. Schematic showing a typical velocity profile for at $x = x_1$, with lower limit for the regression analysis taken at z_{base} (x_1), adjustment height of Δz (x_1), and corresponding displacement height d_* (x_1). Please note that vertical and velocity scales have been exaggerated, and the portion of the velocity profile that was actually resolved is shown by the solid line.

with $d_* = z_{\text{base}} - \Delta z$, where we define Δz as the adjustment height for logarithmic layers that lie between the ripple roughness elements (Figure 9). On a rippled bed, one would expect that (1) at the ripple crests the bed form-induced effects on the velocity profiles are minimal and $d_* \approx z_{\text{base}}$ and (2) at the ripple trough the bed form-induced effects on the velocity profiles are considerable and consequently Δz reaches its maximum. Consistent with visual observations, this formulation also allows for a slip boundary condition to exist at z_{base}.

[44] Substituting for d_* in equation (7), yields

$$u(x,z) = \frac{u_*(x)}{\kappa} \ln\left(\frac{z - z_{\text{base}}(x) + \Delta z(x)}{z_0(x)}\right), \tag{8}$$

for both, first-moment and second-moment statistics. Following *Cox et al*. [1996], *Fredsøe et al*. [1999], and others, least-squares regression to the observations (Figure 8) allows for estimates of u_* (x) and z_0 (x). The lower limits of the regression analysis were located at the first cells above z_{base}, where sediment concentration is assumed to be a maximum by noting that pixels do not saturate below this point. The upper limits of the regression analysis were located at the cell immediately below the velocity overshoot or at the lowest elevation, where $u(x) \geq 0.99u_\infty(x)$. Degrees of freedom (DOF $= n - 2$, with n being the number of points in the regression), for each regression fit are shown in Figure 10a. The adjustment height (Δz, Figure 10c) was found iteratively by increasing Δz by 0.1 mm until the percent difference of the square of the correlation coefficient of the regression (ρ^2, Figure 10b) between consecutive Δz increments was less than or equal to 0.1%. The initial Δz used at every horizontal location was 0.5 mm.

[45] Δz is correlated to the bed elevation (see Figure 10), increasing at the ripple troughs and decreasing at the crests. Δz supports the significance of the bed form-induced pressure gradients and shedding vortices present in the WBBL, while also suggesting a possible significant role of additional spatial gradients.

[46] *Jackson* [1981] showed that d_* is, for a rough boundary, the average level at which the mean drag appears to act. The present analysis results in d_* values located slightly above the ripple trough (min (z_{base}), Table 2). The mean drag appears to act just above the main ripple trough, with standard deviations that are similar in magnitude to half a ripple height ($\eta_b/2$), and suggests a relaxation of the no-slip boundary condition at z_{base} that is not inconsistent with visual observations of significant sediment movement at the ripple crests and slopes. These results suggest that the mean drag on this artificial sediment bed acts closer to the base of the ripple rather than at the expected centroid.

[47] In steady flow, the nondimensional number governing the ratio between the disturbing and stabilizing forces was suggested by *Shields* [1936],

$$\theta_{u_*} \equiv \frac{u_*^2}{(s-1)gd_{50}} \tag{9}$$

where u_* is obtained from the least-squares fit performed in equation (8) and g is the gravitational acceleration. The critical Shields parameter for incipient motion, θ_c, is taken from the modified Shields diagram [*Madsen and Grant*, 1976] as 0.04. For $\theta_{u_*} > 0.8$, the bed is typically considered to have sheet flow conditions and flattens. If we allow u_* to vary spatially, then θ_{u_*} is also spatially variable. Figure 10d shows $\theta_{u_*}(x)$ for onshore, offshore, and standard deviation flows, with vertical bars indicating the standard error of θ_{u_*} with 90% confidence. The values of θ_{u_*} are consistent with a bed within the ripple regime.

[48] In general, the values of θ_{u_*} are comparable with the grain roughness Shields parameter defined in Table 1, where the friction factor is given by *Swart* [1974], following *Nielsen* [1992], *Crawford and Hay* [2001], and *Nichols and Foster* [2007], among others. For irregular waves, the velocity scale used in the $\theta_{2.5}$ expression is usually taken as the significant wave orbital velocity $\left(u_{1/3} = 2u_{\text{rms}}\right)$ [*Maier and Hay*, 2009], which for this effort would yield a value of 0.46, only exceeded by the onshore directed shear stress at the stoss slope of the leftmost ripple crest ($x = 3.5$ cm and $x = 5$ cm). High stress on the stoss slope of the ripple crest is consistent with the direction of bed form migration and is also consistent with the asymmetry of the ripples. Given that the center trough is deeper than the other two, the leftmost ripple may act as a forward facing step during the higher onshore flows.

[49] The overall statistics of θ_{u_*} for the four realizations (Table 2) show significant variability of θ_{u_*} values, as expected due to the highly variable bed elevation. While the θ_{u_*} values tended to increase on the stoss side of the steep ripple, no significant correlation between bed elevation and θ_{u_*} was found. The magnitude of θ_{u_*} obtained from standard deviation velocity profiles is generally smaller than the other two estimates, with standard error significantly lower. This is not surprising given that the standard deviation velocity profiles do not quantify the directional characteristics of the flow field (including the coherent vortices).

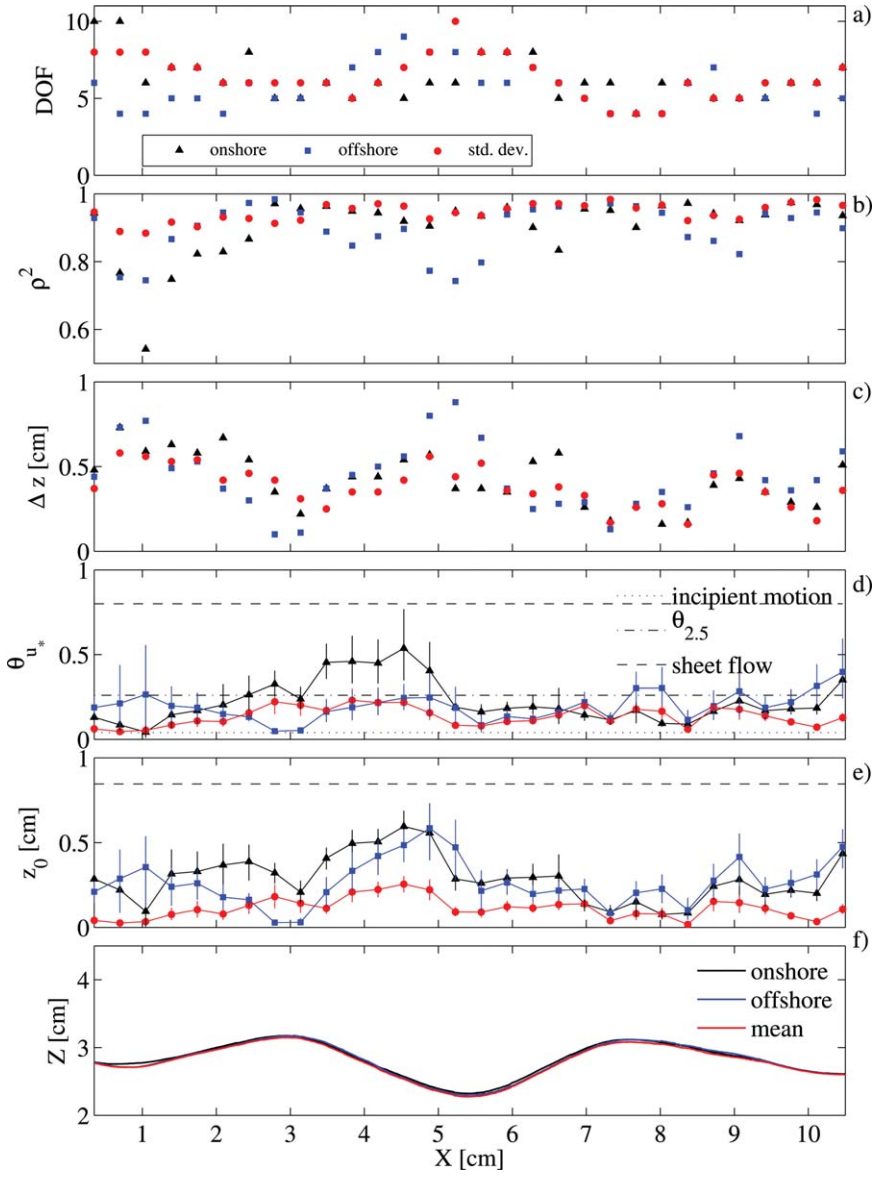

Figure 10. (a–c) Regression parameters including degrees of freedom (DOF), correlation coefficient squared (ρ^2), and adjustment height (Δz). (d) Shields parameter and (e) z_0 at each horizontal position as calculated from the least-squares regression fit over onshore, offshore, and standard deviation velocity profiles for a single realization. Vertical bars indicate the standard error with 90% confidence. The dashed line in Figure 10e indicates one ripple height. (f) z_{base} used as the lower limit of the velocity profiles used in the regression fits.

[50] Both first-moment (onshore and offshore) estimates of z_0 peak at the leftmost ripple trough, specifically at the stoss slope during onshore directed flow, and lee slope during offshore directed flow. Higher order effects induced by asymmetry of the flow and ripples, such as coherent motions and flow acceleration, may contribute to this amplification of z_0. The offshore estimate peaks at $x = 4.9$ cm, consistent with the location of the strongest offshore average of the swirling strength (Figure 4c). Similar to θ_{u_*}, second-moment estimates of z_0, and their standard error, are consistently smaller than the first-moment estimates. Additionally, overall statistics (Table 2) show that the range of z_0 values from second-moment velocity estimates is half the range of the values derived with the first-moment velocity estimates.

[51] In turbulent boundary layers over rough surfaces, we can regard z_0 as a measure of roughness [*Kundu and Cohen*, 2004]. It is common in the WBBL literature to parameterize the bottom roughness with the equivalent Nikuradse roughness (r) defined as $r = 30z_0$ (Table 2). First-moment r estimates are similar for both flow directions and comparable in magnitude to roughness estimates computed with $\theta_{2.5}$ based on the bed load expression for combined waves-currents flow given in *Li et al.* [1997] $(r_{Li} = 522d_{50}(\theta_{2.5} - \theta_c)^{.75} = 9.1\text{cm})$. As with z_0, second-moment estimates are about a factor of 3 lower and in

better agreement with the empirical formulations for bed load roughness given by *Grant and Madsen* [1982] and *Nielsen* [1992], that is, $r_{GM} = 160(s+0.5)d_{50}\theta_c \left(\sqrt{\theta_{2.5}/\theta_c} - 0.7\right)^2 = 2.0\,\text{cm}$ and $r_N = 170 d_{50}\sqrt{\theta_{2.5} - \theta_c} = 4.3\,\text{cm}$. Please note that we have purposely excluded the ripple-induced roughness, since our analysis is concerned with the intraripple flow. Although a formal assessment of r based on theoretical grounds is still required, these results suggest that, in general, the log-layer approach may be able to capture the processes involved in some of the available parameterizations for bed roughness.

9. Discussion: On the Assumption of a Logarithmic Layer

[52] The fundamental assumption in deriving a logarithmic model for the horizontal velocity distribution relies on a no-slip boundary condition at the wall, resulting in a wall shear stress defined by $\tau_0 \equiv \rho u_*^2$. Following *Tennekes and Lumley* [1972], near a smooth wall, there is a small inner layer where molecular diffusion dictates the shape of the velocity profile, and therefore, $u = f(u_*, \nu, z)$. Far away from the wall, but still within the boundary layer, the velocity deficit is primarily due to the turbulent transfer of momentum imposed by the no-slip boundary condition at the wall. It is, therefore, expected that in this outer layer, $u = f(u_*, \delta, z)$. The small overlapping layer where the solutions for both, the inner and outer layers hold, was shown, from purely dimensional arguments by *Millikan* [1938], to follow a logarithmic law. The common logarithmic law for hydrodynamically rough surfaces results from requiring a boundary condition, where $u(z_0) = 0$.

[53] The logarithmic model, while not explicitly requiring steady flows, zero pressure gradients, or a particular stress distribution, is only valid for a small layer, where $u \neq f(\nu, \delta)$. While independence of ν is expected in this hydrodynamically rough environment (Figure 7), the region where the logarithmic regression was performed represents a considerable portion of the boundary layer, roughly 50% when taking δ as the estimate provided by the higher harmonics (O(2) cm). Despite the proximity of the logarithmic layer to δ, and visual observations of a slipping boundary, fitting a logarithmic model to the data yields statistically sound inferences (Figure 10).

[54] We assess the logarithmic layer approach with independent estimates of the momentum transfer within the same layer of thickness $\delta_{\log}$. Similar to *Mellor* [2002], let $\tau_m(x,z) \equiv \overline{|\tau_{xz}(x,z,\tilde{t})|}$ (Figures 11a–11c), where the overbar ($\bar{}$) represents time average and τ_{xz} is the vertical transfer of horizontal momentum, which is approximated by performing a Reynolds decomposition on the velocity and pressure fields, and subsequently phase-averaging the equations of motion. Velocity and pressure are decomposed into

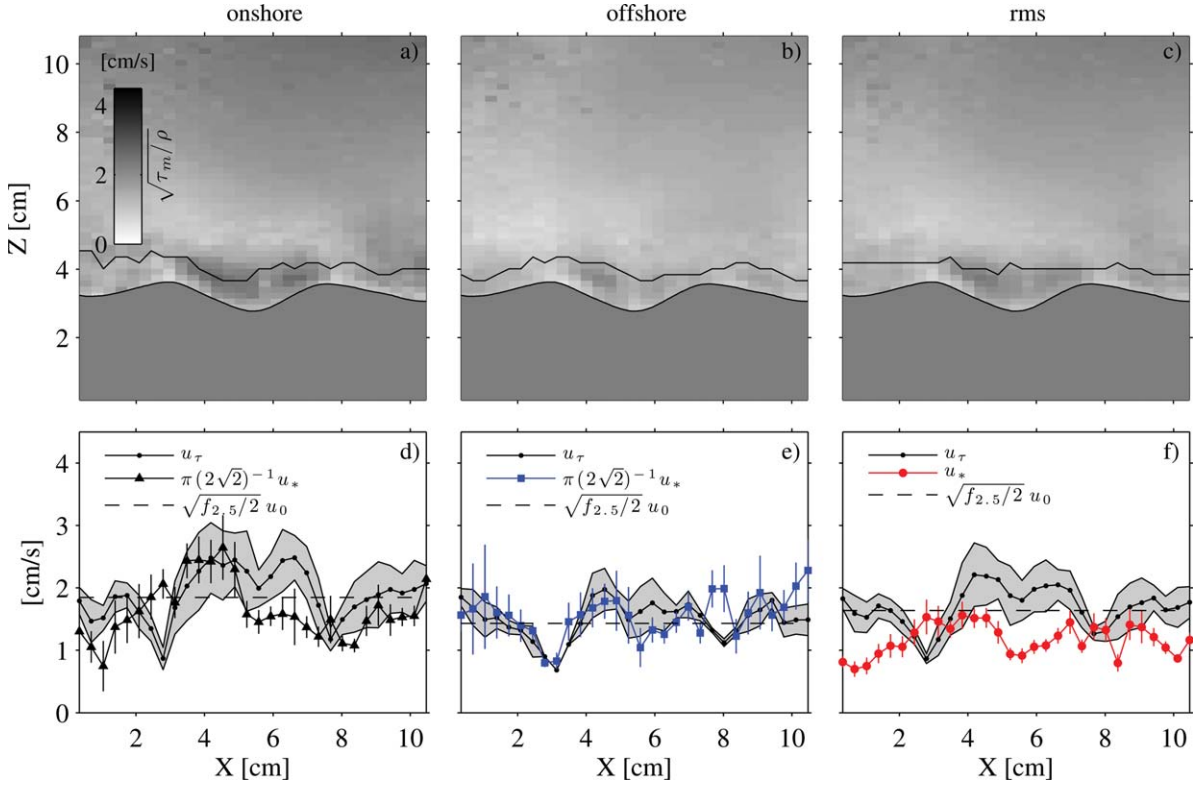

Figure 11. (a) Onshore, (b) offshore, and (c) rms estimates of the time-independent vertical transfer of horizontal momentum as depicted by $\sqrt{\tau_m/\rho}$. Black solid lines represent $\delta_{\log}$. (d) Onshore, (e) offshore, and (f) rms estimates of u_τ (black dotted lines, equation (15), with corresponding variation within $\delta_{\log}$, as computed from the standard deviation (gray shaded area). Values of u_* (equation (8)) and their corresponding error are presented in red (Figures 11d and 11e) and blue (Figure 11f). Empirical estimates of the shear velocity given by $\sqrt{f_{2.5}/2}\,u_0$ (Table 1) are shown by the black dashed line.

mean (current), phase (wave), and fluctuating (turbulent) components defined by

$$u_i \equiv \overline{u}_i + \tilde{u}_i + u_i' \tag{10a}$$

$$p \equiv \overline{p} + \tilde{p} + p' \tag{10b}$$

where overbar ($\bar{}$) represents time average, over tilde ($\tilde{}$) denotes phase average with zero mean, and prime ($'$) represents departure from the latter. Time and phase averages are calculated following *Nielsen* [1992] with

$$\overline{u}_i = \frac{1}{N}\sum_{n=1}^{N} u_i(t_n) \tag{11}$$

$$\tilde{u}_i(\tilde{t}) = \frac{1}{M}\sum_{m=0}^{M} u_i(t+mT) - \overline{u}_i \tag{12}$$

where $N = 720$ is the total number of samples, $M = 30$ is the total number of waves, and $T = 2$ s is the wave period.

[55] Substituting equation (10a)–(10b) in the Navier-Stokes equations for incompressible flow in Cartesian tensor notation, and taking the phase average yields

$$\frac{\partial \tilde{u}_i}{\partial \tilde{t}} + \frac{\partial \tilde{u}_i \tilde{u}_j}{\partial x_j} + \frac{\partial \widetilde{u_i' u_j'}}{\partial x_j} = -\frac{1}{\rho}\frac{\partial \tilde{p}}{\partial x_i} + \nu \frac{\partial^2 \tilde{u}_i}{\partial x_j \partial x_j}, \tag{13}$$

where it has been assumed that the mean quantities are negligible (Figure 4e). In Cartesian coordinates, the terms that represent the vertical transfer of horizontal momentum [*Nielsen*, 1992] are given by

$$\tau_{xz}(x,z,\tilde{t}) = \mu\frac{d\tilde{u}}{dz} - \rho\tilde{u}\tilde{w} - \rho\widetilde{u'w'}, \tag{14}$$

where the first term represents the viscous stress, the second term is the "wave" stress, and the third term is the Reynolds stress. In contrast to Mellor's expression, which was originally developed for rigid lid oscillatory flows and flat beds ($\tilde{w} = 0$), equation (14) includes the effects of both, bed form-induced acceleration/deceleration and bed form-induced coherent motions, given by the highly correlated term $\rho\tilde{u}\tilde{w}$. The corresponding shear velocity is defined as

$$u_\tau^2(x) \equiv \frac{1}{\rho\delta_{\log}}\int_{z_b}^{z_b+\delta_{\log}} \tau_m(x,z)\mathrm{d}z. \tag{15}$$

[56] This approach for computing u_τ provides for a direct comparison with values of u_* inferred from the log-layer fits to the rms velocity signal (or u_{std} with zero mean, Figure 11f). Please note that while there appears to be a signal at the upper left corner of the rms τ_m (Figure 11c), it does not affect the u_τ estimates, since the integration only includes elevations below $\delta_{\log}$. Additionally, comparisons with half-wave averages require a modulation of $\pi(2\sqrt{2})^{-1}$ since the rms of a half-wave period is mathematically different from the average (Figures 11d and 11e). It is also worth noting that the positive definition of τ_m does not allow for partitioning of u_τ between the viscous, wave, and turbulent components.

[57] Shear velocity comparisons generally show consistency between the two methods (rms deviations of 0.53, 0.35, and 0.57 cm s^{-1} for the onshore, offshore, and rms cases, respectively). Both estimates are considerably close to empirical formulations for u_* given by the wave friction factor $f_{2.5}$, which only takes into account the grain roughness ($2.5d_{50}$).

[58] Shear velocities inferred from the vertical transfer of horizontal momentum (u_τ) are consistently weaker at the ripple crests. This is expected since the flow above the crests is nearly horizontal, and consequently $\tilde{u}\tilde{w}$ is a minimum, and suggests that the small-scale turbulence is the main mechanism responsible for the vertical transfer of momentum above the ripple crests. At the stoss and lee slopes, u_τ increases due to flow acceleration and formation of coherent structures, respectively.

[59] While the offshore half-wave period is slightly longer and weaker than the onshore, Figures 4b and 4c suggest that the bed form-induced flow structures are slightly more coherent and organized during the offshore-directed flow. This may influence the estimates of $\tilde{u}\tilde{w}$, and consequently may account for the agreement between u_* and u_τ at the stoss slope during the offshore directed flow. The estimates of u_* and u_τ from rms velocity statistics (Figure 11f) are of similar magnitude, but can disagree by as much as a factor of 2. Their spatial mismatch is expected, as the rms velocity signal is not able to capture the nearbed directional-dependence associated with the coherent structures.

[60] The results above suggest that (1) Small-scale turbulence, as accounted for with the Reynolds decomposition, is not the only mechanism responsible for transferring momentum within the logarithmic layer, and therefore contributions from $\tilde{u}\tilde{w}$ must be included for rippled beds; (2) Spatial correlation between u_τ and u_* for the longer and weaker offshore half-wave period suggest that the flow may be more similar to a steady flow environment, where flow acceleration effects are less significant. This is in contrast to the lack of spatial correlation during the shorter duration high-acceleration onshore half-wave period; and (3) While intraripple measurements of the WBBL may not account for the entire drag, they provide for estimates that are similar in magnitude to the grain roughness-induced skin friction, however, spatial variability can be more than a factor of 2.

10. Summary and Concluding Remarks

[61] New detailed observations of the 2-D velocity field over a mobile rippled bed subjected to slightly skewed and asymmetric wave forcing conditions are presented in this paper. The intraripple spatial characterizations of the hydrodynamics within the WBBL are examined in the time and frequency domains, and with first-moment and second-moment velocity statistics.

[62] Spectral analysis of the horizontal velocity field obtained from PIV showed that spectral energy vertically decays at the zeroth and first harmonics (f_0 and $2f_0$), but is significantly intensified at the second harmonic ($3f_0$) near the ripple slopes, where vortices occur. Cross-spectral analysis showed a phase separation at the zeroth harmonic that

is mostly consistent with vortex signatures, provided by the swirling strength. Stronger phase separation at the second harmonic is not inconsistent with previous flat bed efforts, yet its higher magnitude is attributed to bed form-induced pressure gradients.

[63] First-moment (onshore and offshore directed flow) and second-moment (standard deviation flow) statistics were used to infer spatially variable hydrodynamic quantities. Integral (displacement and momentum thickness) and differential (viscous shear stress) flow characteristics show sensitivity at illustrating the impact of a rippled boundary in the surrounding flow field. The estimates of boundary layer thickness show signatures of adverse pressure gradients and wakes in the troughs and lee side of the ripples, and shrunken boundary layers at the ripple crests. The integral approaches, while useful for characterizing flow separation, provide estimates of boundary layer thickness that are much smaller than suggested by the higher harmonics and vertical velocity gradients.

[64] Fitting a logarithmic model to first-moment and second-moment velocity profiles between ripple elements provides estimates of shear stress, mean drag elevation, and bed roughness. Shear stresses characterized by the Shields parameter locate the bed within the ripple regime, and suggest stress amplification at the stoss slope of asymmetric ripples during the strongest flow direction (onshore). The mean drag, while not formally quantified in this effort, appears to act slightly above the ripple trough and not at the expected centroid of the ripple, based on the interpretation of d_* by *Jackson* [1981].

[65] An assessment of z_0 estimates indicates an increased bed roughness for first-moment velocity statistics that is well modeled by the empirical expression given in *Li et al*. [1997]. The second-moment statistics provide roughness estimates that are roughly a factor of 3 lower, and in better agreement with formulations by *Grant and Madsen* [1982] and *Nielsen* [1992]. Our results imply that the logarithmic layer approach and empirical bed load parameterizations may be able to properly capture the quasi-steady intraripple flow characteristics at most locations along the rippled bed, but that the logarithmic model localized to a single position does not accurately represent the dynamics over the entire ripple.

[66] The logarithmic formulation is evaluated with direct estimates of the near-bed momentum transfer based on the work of *Mellor* [2002]. Both approaches yield stress estimates that fluctuate about the mean skin friction based on the grain roughness wave friction factor. Vertical transfer of horizontal momentum, including flow acceleration/deceleration and coherent vortices, is well captured by logarithmic fits to intraripple velocity profiles only during the longer and weaker offshore half-wave period. The comparisons using rms velocity profiles show little to no correlation, suggesting that intraripple directional information may be lost when using this approach.

[67] **Acknowledgments.** This work was supported by the National Science Foundation (CTS-0348203) and the Department of Defense through the National Defense Science & Engineering Graduate Fellowship Program. The authors are very grateful to the TUDelft Fluids Mechanics Laboratory Professors (M. Stive and A. Reniers), staff and students. Also, this work was possible with assistance of members of the OSU Coastal Transport Laboratory (G. Smith, G. Margelowsky, and D. Frank) and the UNH Ocean Engineering Program (J. Irish, T. Lippmann, and P. Bachant). Finally, the authors would like to thank the anonymous reviewers, whose careful comments helped improve the manuscript substantially.

References

Ahmed, A. S. M., and S. Sato (2001), Investigation of bottom boundary layer dynamics of movable bed by using enhanced PIV technique, *Coastal Eng. J.*, *43*(4), 239–258.

Ayrton, H. (1910), The origin and growth of ripple-mark, Proc. R. Soc. London, Ser. A, *84*(571), 285–310.

Bagnold, R. A. (1946), Motion of waves in shallow water, interaction between waves and sand bottoms, Proc. R. Soc. London, Ser. A, *187*(1008), 1–18.

Beji, S., and J. Battjes (1993), Experimental investigation of wave propagation over a bar, *Coastal Eng.*, *19*(1), 151–162.

Bertuccioli, L., G. Roth, J. Katz, and T. Osborn (1999), A submersible particle image velocimetry system for turbulence measurements in the bottom boundary layer, *J. Atmos. Oceanic Technol.*, *16*(11), 1635–1646.

Chang, Y. S., and D. M. Hanes (2004), Suspended sediment and hydrodynamics above mildly sloped long wave ripples, *J. Geophys. Res.*, *109*, C07022, doi:10.1029/2003JC001900.

Cheng, N. (2009), Comparison of formulas for drag coefficient and settling velocity of spherical particles, *Powder Technol.*, *189*(3), 395–398.

Coleman, S. E., V. I. Nikora, and T. Schlicke (2008), Spatially-averaged oscillatory flow over a rough bed, *Acta Geophys.*, *56*(3), 698–733.

Cowen, E. A., I. M. Sou, P. L. Liu, and B. Raubenheimer (2003), Particle image velocimetry measurements within a laboratory-generated swash zone, *J. Eng. Mech.*, *129*(10), 1119–1129.

Cox, D., N. Kobayashi, and A. Okayasu (1994), Vertical variations of fluid velocities and shear stress in surf zones, paper presented at 24th International Conference on Coastal Engineering, Am. Soc. of Civ. Eng., Kobe, Japan.

Cox, D., N. Kobayashi, and A. Okayasu (1996), Bottom shear stress in the surf zone, *J. Geophys. Res.*, *101*(C6), 14,337–14,348.

Crawford, A. M., and A. E. Hay (2001), Linear transition ripple migration and wave orbital velocity skewness, *J. Geophys. Res.*, *106*, 14,113–14,128.

Darwin, G. H. (1883), On the formation of ripple-mark in sand, Proc. R. Soc. London, *36*, 18–43.

Davies, A., and P. Thorne (2005), Modeling and measurement of sediment transport by waves in the vortex ripple regime, *J. Geophys. Res.*, *110*, C05017, doi:10.1029/2004JC002468.

Doering, J., and A. Baryla (2002), An investigation of the velocity field under regular and irregular waves over a sand beach, *Coastal Eng.*, *44*(4), 275–300.

Dong, R., S. Chu, and J. Katz (1992), Quantitative visualization of the flow within the volute of a centrifugal pump. i: Technique, *J. Fluids Eng.*, *114*(3), 390–395.

Doron, P., L. Bertuccioli, J. Katz, and T. R. Osborn (2000), Turbulence characteristics and dissipation estimates in the coastal ocean bottom boundary layer from PIV data, *J. Phys. Oceanogr.*, *31*, 2108–2134.

Doucette, J. (2002), Bedform migration and sediment dynamics in the nearshore of a low-energy sandy beach in southwestern Australia, *J. Coastal Res.*, *18*(3), 576–591.

Doucette, J., and T. O'Donoghue (2006a), Response of sand ripples to change in oscillatory flow, *Sedimentology*, *53*(3), 581–596.

Doucette, J. S., and T. O'Donoghue (2006b), Response of sand ripples to change in oscillatory flow, *Sedimentology*, *53*, 581–596.

Drake, D., and D. Cacchione (1986), Field observations of bed shear stress and sediment resuspension on continental shelves, Alaska and California, *Cont. Shelf Res.*, *6*(3), 415–429.

Drake, D., D. Cacchione, and W. Grant (1992), Shear stress and bed roughness estimates for combined wave and current flows over a rippled bed, *J. Geophys. Res.*, *97*(C2), 2319–2326.

Efron, B., and R. J. Tibshirani (1993), *An Introduction to the Bootstrap*, Chapman and Hall, Boca Raton, La.

Elfrink, B., D. Hanes, and B. Ruessink (2006), Parameterization and simulation of near bed orbital velocities under irregular waves in shallow water, *Coastal Eng.*, *53*(11), 915–927.

Elgar, S., and R. Guza (1985), Observations of bispectra of shoaling surface gravity waves, *J. Fluid Mech.*, *161*, 425–448.

Foster, D. L., R. A. Beach, and R. A. Holman (2000), Field observations of the wave bottom boundary layer, *J. Geophys. Res.*, *105*(C8), 19,631–19,647.

Foster, D. L., A. J. Bowen, R. A. Holman, and P. Natoo (2006), Field evidence of pressure gradient induced incipient motion, *J. Geophys. Res.*, *111*, C05004, doi:10.1029/2004JC002863.

Fredsøe, J., and R. Deigaard (1992), *Mechanics of Coastal Sediment Transport*, World Sci, Singapore.

Fredsøe, J., K. H. Andersen, and B. M. Sumer (1999), Wave plus current over a rippled-covered bed, *Coastal Eng.*, *38*, 177–221.

Gimenez-Curto, L. A., and M. A. Corniero Lera (1996), Oscillating turbulent flow over very rough surfaces, *J. Geophys. Res.*, *101*(C9), 20,745–20,758.

Gonzalez-Rodriguez, D., and O. Madsen (2007), Seabed shear stress and bedload transport due to asymmetric and skewed waves, *Coastal Eng.*, *54*(12), 914–929.

Grant, W. D., and O. Madsen (1982), Movable bed roughness in unsteady oscillatory flow, *J. Geophys. Res.*, *87*(C1), 469–481.

Hassan, W., and J. Ribberink (2005), Transport processes of uniform and mixed sands in oscillatory sheet flow, *Coastal Eng.*, *52*(9), 745–770.

Henriquez, M., A. J. H. M. Reniers, B. G. Ruessink, M. J. F. Stive, T. P. Stanton, and D. L. Foster (2008), On the scaling of sediment transport in the nearshore, paper presented at International Conference on the Application of Physical Modeling to Port and Coastal Protection, Bari, Italy. International Association of Hydro-Environment Engineering and Research (IAHR).

Huang, H., D. Dabiri, and M. Gharib (1999), On errors of digital particle image velocimetry, *Meas. Sci. Technol.*, *8*(12), 1427–1440.

Jackson, P. (1981), On the displacement height in the logarithmic velocity profile, *J. Fluid Mech.*, *111*(1), 15–25.

Jonsson, I., and N. Carlsen (1976), Experimental and theoretical investigations in an oscillatory turbulent boundary layer, *J. Hydraul. Res.*, *14*(1), 45–60.

Keane, R., and R. Adrian (1992), Theory of cross-correlation analysis of PIV images, *Appl. Sci. Res.*, *49*(3), 191–215.

Kundu, P., and I. Cohen (2004), *Fluid Mechanics*, Academic, San Diego, Calif.

Li, M. Z. L. (1994), Direct skin friction measurements and stress partitioning over movable sand ripples, *J. Geophys. Res.*, *99*(C1), 791–799.

Li, M., C. Amos, and D. Heffler (1997), Boundary layer dynamics and sediment transport under storm and non-storm conditions on the Scotian shelf, *Mar. Geol.*, *141*(1), 157–181.

Maddux, T., S. McLean, and J. Nelson (2003), Turbulent flow over three-dimensional dunes: 2. Fluid and bed stresses, *J. Geophys. Res.*, *108*(F1), 6010, doi:10.1029/2003JF000018.

Madsen, O. S., and W. D. Grant (1976), Quantitative description of sediment transport by waves, in *Fifteenth International Conference on Coastal Engineeering*, vol. *2*, pp. 1093–1112, Am. Soc. of Civil Eng, Honolulu, Hawaii.

Maier, I., and A. Hay (2009), Occurrence and orientation of anorbital ripples in near-shore sands, *J. Geophys. Res.*, *114*, F04022, doi:10.1029/2008/JF001126.

Maxey, M. (1987), The gravitational settling of aerosol particles in homogeneous turbulence and random flow fields, *J. Fluid Mech.*, *174*(1), 441–465.

Mellor, G. (2002), Oscillatory bottom boundary layers, *J. Phys. Oceanogr.*, *32*(11), 3075–3088.

Millikan, C. (1938), A critical discussion of turbulent flows in channels and circular tubes, in *Proceedings of the 5th International Congress for Applied Mechanics*, Cambridge, Mass., pp. 386–392, John Wiley, New York.

Nelson, J. M., and J. D. Smith (1989), Mechanics of flow over ripples and dunes, *J. Geophys. Res. Oceans*, *94*(C6), 8146–8162.

Nichols, C. S., and D. L. Foster (2007), Full-scale observations of wave-induced vortex generation over a rippled bed, *J. Geophys. Res.*, *112*, C10015, doi:10.1029/2006JC003841.

Nichols, C. S., and D. L. Foster (2009), Observations of bed form evolution with field-scale oscillatory hydrodynamic forcing, *J. Geophys. Res.*, *114*, C08010, doi:10.1029/2008JC004733.

Nielsen, P. (1986), Suspended sediment concentrations under waves, *Coastal Eng.*, *10*(1), 23–31.

Nielsen, P. (1992), *Coastal Bottom Boundary Layers and Sediment Transport*, World Sci, Singapore.

Nielsen, P. (2006), Sheet flow sediment transport under waves with acceleration skewness and boundary layer streaming, *Coastal Eng.*, *53*(9), 749–758.

Nimmo Smith, W. A. M., J. Katz, and T. R. Osborn (2005), On the structure of turbulence in the bottom boundary layer of the coastal ocean, *J. Phys. Oceanogr.*, *35*, 72–92.

Ning, D., X. Zhuo, L. Chen, and B. Teng (2012), Nonlinear numerical investigation on higher harmonics at lee side of a submerged bar, *Abstr. Appl. Anal.*, *2012*, ID 214897, doi: 10.1155/2012/214897.

O'Donoghue, T., and G. Clubb (2001), Sand ripples generated by regular oscillatory flow, *Coastal Eng.*, *44*(2), 101–115.

O'Donoghue, T., J. S. Doucette, J. J. van der Werf, and J. S. Ribberink (2006), The dimensions of sand ripples in full-scale oscillatory flows, *Coastal Eng.*, *53*, 997–1012.

Osborne, P. D., and C. E. Vincent (1996), Vertical and horizontal structure in suspended sand concentrations and wave-induced fluxes over bedforms, *Mar. Geol.*, *131*, 195–208.

Raffel, M., C. Willert, and S. Wereley (2007), *Particle Image Velocimetry: A Practical Guide*, Springer, Berlin.

Rodriguez-Abudo, S. (2011), Characterization of the wave bottom boundary layer over movable rippled beds, MS thesis, Univ. of N. H, Durham, N. H.

Schlichting, H. (1979), *Boundary-Layer Theory*, 7th ed., McGraw-Hill, New York.

Shaw, W., and J. Trowbridge (2001), The direct estimation of near-bottom turbulent fluxes in the presence of energetic wave motions, *J. Atmos. Oceanic Technol.*, *18*(9), 1540–1557.

Shields, A. (1936), Anwendung der anhlichkeitsmechanik und turbulenzforschung auf die geschiebebewegung, Mitt. Preuss Versuchsanst. Wassebaur Schiffbau, 1–26.

Sleath, J. F. A. (1987), Turbulent oscillatory flow over rough beds, *J. Fluid Mech.*, *182*, 369–409.

Sleath, J. F. A. (1999), Conditions for plug formation in oscillatory flow, *Cont. Shelf Res.*, *19*, 1643–1664.

Smyth, C., A. E. Hay, and L. Zedel (2002), Coherent doppler profiler measurements of near-bed suspended sediment fluxes and the influence of bed forms, *J. Geophys. Res.*, *107*(C8), 3105, doi:10.1029/2000JC000760.

Sveen, J. K. (2004), *An Introduction to MatPIV 1.6.1*, 2nd ed., Dep. of Math., Univ. of Oslo, Oslo.

Swart, D. H. (1974), Offshore sediment transport and equilibrium beach profiles, *Publ. 131*, Delft Hydraul. Lab, Delft, the Netherlands.

Tennekes, H., and J. Lumley (1972), *A First Course in Turbulence*, MIT Press, Cambridge, Mass.

Thorne, P. D., and D. M. Hanes (2002), A review of acoustic measurement of small-scale sediment processes, *Cont. Shelf Res.*, *22*, 603–632.

Traykovski, P., A. E. Hay, J. D. Irish, and J. F. Lynch (1999), Geometry, migration, and evolution of wave orbital ripples at leo-15, *J. Geophys. Res.*, *104*(C1), 1505–1524.

Trowbridge, J. H., and Y. C. Agrawal (1995), Glimpses of a wave boundary layer, *J. Geophys. Res.*, *100*(C10), 20,729–20,745.

Trowbridge, J., and S. Lentz (1998), Dynamics of the bottom boundary layer on the northern California shelf, *J. Phys. Oceanogr.*, *28*(10), 2075–2093.

Van den Boomgaard, M. J. G. (2003), Wave focussing in a laboratory flume, MS thesis, Delft Univ. of Technol., Delft, the Netherlands.

van der A. D., T. O'Donoghue, A. Davies, and J. Ribberink (2011), Experimental study of the turbulent boundary layer in acceleration-skewed oscillatory flow, *J. Fluid Mech.*, *684*, 251–283.

Van der Werf, J. J., J. S. Doucette, T. O'Donoghue, and J. S. Ribberink (2007), Detailed measurements of velocities and suspended sand concentrations over full-scale ripples in regular oscillatory flow, *J. Geophys. Res.*, *112*, F02012, doi:10.1029/2006JF000614.

White, F. (1994), *Fluid Mechanics*, McGraw-Hill, New York.

Wiberg, P. L., and J. M. Nelson (1992), Unidirectional flow over asymmetric and symmetrical ripples, *J. Geophys. Res.*, *97*(C8), 12,745–12,761.

Zhou, J., R. J. Adrian, S. Balachandar, and T. M. Kendall (1999), Mechanisms for generating coherent packets of hairpin vortices in channel flow, *J. Fluid Mech.*, *387*, 353–396.